Unmanned Systems, Vol. 7, No. 4 (2019) 195–213

DOI: 10.1142/S2301385019500067

UNMANNED SYSTEMS
http://www.worldscientific.com/worldscinet/us

Design of a Hybrid Aerial Robot with Multi-Mode Structural Efficiency and Optimized Mid-Air Transition

Jun En Low*, Danial Sufiyan†, Luke Soe Thura Win‡,
Gim Song Soh§, Shaohui Foong¶

Engineering Product Development Pillar,
Singapore University of Technology and Design,
8 Somapah Road, Singapore 487372, Singapore

In this paper, we explore a novel multi-mode hybrid Unmanned Aerial Vehicle (UAV). We combine a tailless fixed-wing with a dual-wing monocopter such that the craft's propulsion systems and aerodynamic surfaces are fully utilized in both a horizontal cruising mode and a vertical hovering mode. This maximizes the structural efficiency across the flight envelope, thereby reducing drag and unused mass while airborne in either flight mode. This UAV is also designed such that the transition between the two flight modes can be executed in mid-air, using only its existing flight actuators and sensors — there are no transition specific actuators. Using two prototypes, the foundational design and control of the system is established; the first explores the hovering mode characteristics of the unique dual-wing monocopter configuration, while the second explores the full multi-mode capabilities of the combined platform. In addition to analytical simulations, the prototypes are experimentally evaluated and assessed to demonstrate the feasibility, viability and potential of this multi-mode aerial robot design.

Keywords: Aerial robots; system design; under-actuated system.

1. Introduction

Across a broad range of unmanned aerial vehicle (UAV) applications, it is useful for a UAV design to possess both a cruising and a hovering flight mode. The former provides higher speeds and longer range while the latter provides functionality and maneuverability to traverse constrained and enclosed environments. For example, in first responder applications, the UAV would, need to possess a rapid response time over long distances while also being able to hover at any point in the mission — be it over mountains, jungles or water bodies, for the retrieval or delivery of material or personnel. Another example would be in the courier business, where service providers can tap on the longer range to reduce the number of aerodromes needed to cover a region while also allowing said regions to include dense urban areas where traditional runways are not available.

As appealing as these capabilities may be, combining a cruising mode and a hovering mode onto a single platform poses several significant design challenges. The most inherent of these is that current solutions tend to have a high degree of structural inefficiency — the propulsion systems and aerodynamic surfaces are not fully utilized in both flight modes. This is due to the fundamentally different operating principles of cruising and hovering flight; efficient cruising flight is optimized around linear airflow as compared to hovering flight, which has a larger contribution from rotational airflow. This often leads to numerous single-mode only components that eat into flight efficiency by being an inefficient mass or by being an additional source of aerodynamic drag. Even worse, additional components might be needed to execute the transition step between the two flight modes, further adding to the mass and mechanical complexity of the platform.

Received 17 October 2018; Revised 15 April 2019; Accepted 15 April 2019; Published 3 September 2019. This paper was recommended for publication in its revised form by editorial board member, Stephen D. Prior.
Email Addresses: *junen_low@sutd.edu.sg, †danial_sufiyan@sutd.edu.sg, ‡thura_soe@sutd.edu.sg, §sohgimsong@sutd.edu.sg, ¶foongshaohui@sutd.edu.sg

Efforts to reduce single-mode only components to improve the structural efficiency of hybrid aircraft have had a good measure of success. A manned example of this would be the V-22 Osprey which uses the same propulsion systems for both cruising and hovering flight. While much of its wing surfaces are still single-mode only and it requires additional mechanisms for its transition step, the design is nevertheless a strong testament for hybrid aircrafts. As compared to its purely rotor-winged predecessor, the CH-46 Sea Knight, it has almost triple the combat radius and twice the cruising speed, all while retaining similar hover capabilities [1, 2].

Within the field of UAVs, we see a greater variety of solutions to improving structural efficiency as the absence of an on-board crew eliminates the need to follow specific orientations for forward flight and allows for a larger mass budget for other components. Some examples in contrast to the Osprey can be seen in Fig. 1.

Structural efficiency can be defined as a property of a multi-mode aircraft, and can be expressed mathematically as

$$\frac{A_u}{A_{\mathrm{Tot}}} \times 100\%, \tag{1}$$

where A_u is the aerodynamically functional area (wings, flaps, propellers, etc.) utilized in all modes, and A_{Tot} is the total aerodynamically functional area of the aircraft. Totally independent systems for each mode would have a 0% structural efficiency, while a craft with a shared system used for all modes would yield a structural efficiency of 100%.

On the low end of the spectrum, we have designs that fuse a multi-rotor frame onto a separate fixed-winged frame. While structurally inefficient, they are mechanically simpler than other hybrids, making them a viable test bed for exploring use cases. Toward the middle, we see more optimized designs that use additional mechanisms to rotate some or all of their propulsion systems (much like the Osprey) to ensure at least some of the components are utilized in both flight modes. And finally, toward the limit of structural efficiency, we have hybrids like the tail-sitter that do away with the added transition mechanisms and instead rotate the entire craft via a pitching maneuver.

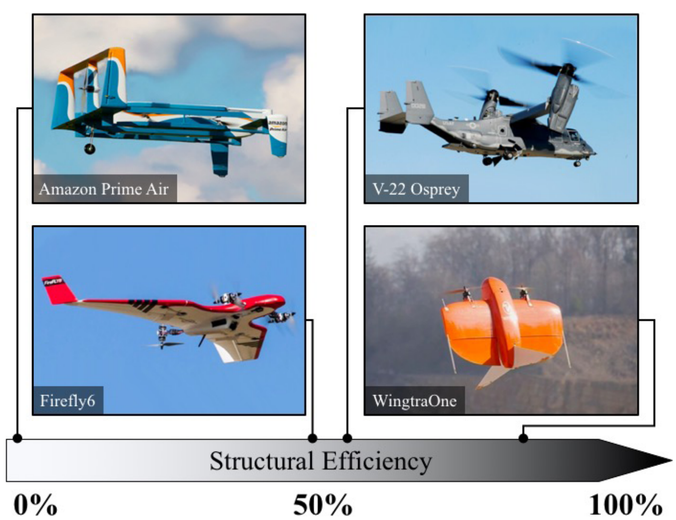

Fig. 1. Structural efficiency comparison of various multi-mode aircraft designs.

However, in all the designs mentioned above, the wing surfaces that are the hallmark of the cruising mode are still inhibitive, if not unused, in the hovering mode. Moreover, all the above categories also use their propulsion systems to directly counter gravity when in the hovering mode resulting in a high disc loading which in turn contributes to a poor hover efficiency.

To tackle this, we seek a hybrid configuration that can retain the use of the wings in hovering flight, thereby maximizing structural efficiency in a way that keeps the disc loading low. Taking inspiration from the tail-sitter, we take the pilot-less advantage further by choosing a design that also disregards the need for a constant forward orientation within the hovering flight mode itself. Known as a monocopter, this aircraft design rotates its entire fuselage as a wing to generate lift.

1.1. *A brief on monocopters*

Monocopters are not a new concept. Nature has been its earliest proponent with an existing example being the samara seed, a winged achene that utilizes its entire body to generate lift. Studies like [3, 4] have shown that these seeds possess excellent, passive lift generating properties (autorotation), are inherently stable and can be controlled.

Given these attractive characteristics, man-made versions added propulsion systems to enable sustained flight and flaps for directional control. An early example of these would be the Gyroptre, a giant, manned prototype by Alphonse Papin and Didier Rouilly [5] from the 1910s. While this prototype didn't take off (both literally and figuratively), it marked the beginning of researchers' attempts to develop a structurally efficient, hover capable aircraft.

The start of the 21st century saw the revival of the monocopter concept. Hoburg and Houghton developed a prototype in 2008 that could repeatably fly across a 70 m by 3 m corridor followed by a 1.5 m doorway [6], thereby proving its viability for use in confined spaces. Hoburg and Houghton also made two important advances. The first was the observation that with proper selection of design parameters, a propulsion system and flap equipped monocopter can still achieve a passive stability in hover akin to its samara seed ancestors. The second was the linking of this nature inspired design to helicopter dynamic and control principles; for example, the control advantages of using a fixed angular velocity for the rotor and the cyclic actuation solutions for forward flight.

The properties that give the monocopter astounding structural efficiency also gives it its drawbacks. The constantly rotating fuselage hinders certain popular and useful payloads like video cameras as they tend to be rotation sensitive. Such payloads would require either additional mechanical components or a software solution (like [7, 8]) to stabilize the heading of the sensor. The former leads to added mass and added mechanical complexity, while the latter is highly dependent on environmental brightness and on-board nutation. More critically, both actuated and non-actuated solutions are proportionally harder to implement the higher the hover angular velocity as the sensor and control would have to be more precise (thereby posing an additional challenge to scaling down the design).

That said, these drawbacks should not be reason enough to disregard the design. A multitude of rotation insensitive payloads exist; gas sensors, wireless signal relays, Global Position Systems (GPS), first-aid kits, fertilizers and pesticides just to name a few. In fact, there also exist sensors that could benefit from a controlled angular velocity like spinning Light Detection and Ranging (LIDAR) sensors and event-based cameras.

As such, we believe there are good motivations for exploring monocopter designs and their potential use cases. Given the structural similarity of a dual-wing monocopter to a tailless fixed-wing, we believe that monocopters have an especially compelling case within the field of hybrid UAVs. To simplify terminology, we henceforth call such a hybrid a Transfomable HOvering Rotorcraft (THOR). With their ability to keep the wings fully utilized in both its dual-wing monocopter configuration and its tailless fixed-wing configuration, we hypothesize that such a design can possess two regions of flight efficiency within its flight envelope as compared to the single region of common hybrid designs like the tailsitter (Fig. 2).

1.2. *Summary of contributions*

As a first step toward investigating our hypothesis, we make the following contributions:

- A comprehensive dynamic model for a dual-wing monocopter that uses 2nd order rotational symmetry to simplify design and control. This forms the foundation of the craft's hovering mode.
- Control solutions for the dual-wing monocopter flight mode. We utilize helicopter control principles to influence both the hardware and software aspects of flight control in hovering mode.

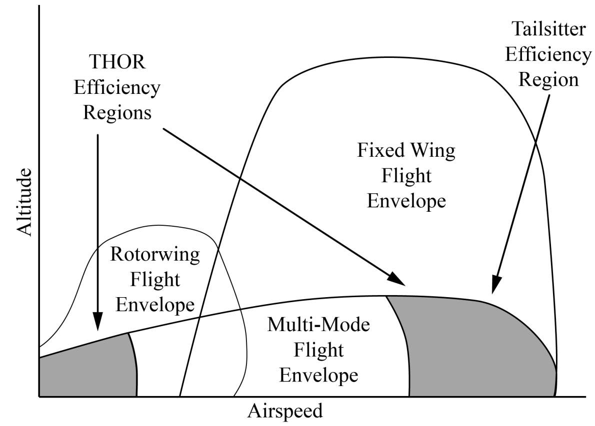

Fig. 2. Target efficiency regions of flight of a THOR multi-mode UAV as compared to other multi-mode designs. Note the rotor wing and fixed wing flight envelopes for contrast.

- An additional dynamic model unique to the transition step. Given the extremities of flight conditions within the transition step, we utilize a separate model for this phase that is built on a different set of simplifying assumptions.
- A control solution for the forward transition (FT) (hovering to cruising). Given the large angular velocities unique to the hover mode, an FT without a controller is both unreliable and dangerous. We describe a multi-phased control solution that ensures a repeatable, robust mid-air transition without the use of additional components.
- A long-term software build that would allow for further expansion of research on the platform.

Note that we do not delve deep into the modeling of the cruising mode in this paper as it is nearly identical to the fixed-wing mode of tailsitters, whose model and control is already well described in the existing literature like [9, 10]. Design constraints necessary for stable flight in this fixed-wing mode were achievable without any conflict with the hovering mode contributions we made. In fact, we were able to conduct succesful orbiting flight tests in the fixed-wing mode (Sec. 3.5) with only minor tuning to existing flight controller software (PX4 VTOL and KK VTOL).

2. The Transformable HOvering Rotorcraft (THOR)

A 2nd order, rotationally symmetric, dual-wing monocopter is strikingly similar to a tailless fixed-wing, the only difference being that the wings are collectively π radians apart in the monocopter setup. By splitting the actuation into almost equal components ($\frac{\pi}{2}$ radians for each wing), we have been able to develop prototypes [11–13] that can execute a

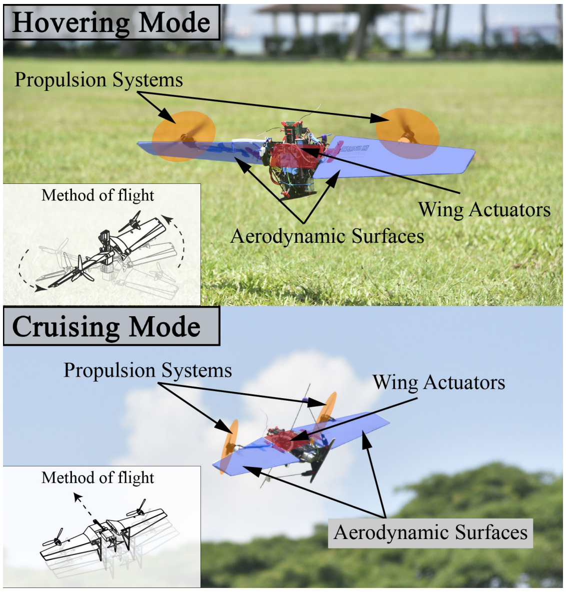

Fig. 3. THOR prototype from [11] with aerodynamic surfaces and propulsion systems highlighted.

transition with minimal component travel that uses already existent flight actuation mechanisms. Hence, our propulsion systems and aerodynamic surfaces remain fully utilized, as illustrated below in Fig. 3.

The 2nd order rotational symmetry provides two other benefits. Firstly, it ensures that the majority of forces and torques that the craft experiences have an opposite component whose magnitude we can vary. This gives us options for control. Secondly, it helps to keep the inertia tensor mostly diagonal with a large component in the axis of rotor rotation. This gives the craft a degree of passive stability (More on this in Sec. 2.2).

Improving on our previous works, we implement an additional adaptation of helicopter dynamics and control-separated cyclic and collective pitch control. In helicopter control, a collective pitch increases the pitch angle of all rotor blades by the same amount, thereby increasing rotor thrust (altitude control). A cyclic pitch increases the pitch angle of each rotor blade depending on its angle with the forward direction of the craft. This produces a torque which can be used to impart a lateral or longitudinal velocity (pitch/roll control). Their separation allows for the simplification of modeling as we can use a fixed rotor angular velocity assumption. It also simplifies the control by decoupling altitude and pitch/roll control. We take this one step further by separating not only their calculation but also their output actuator mechanisms — we use a high torque, low speed servo system for the collective and a low torque, high speed servo system for the cyclic. This essentially gives us an electronically equivalent but mechanically simplified swashplate.

2.1. *Monocopter dynamic model*

In this section, we describe a simple but insightful dynamic model of our monocopter. This model differs from previous contributions like [14, 15] and [16] as it accounts for the craft's larger wing area, which makes small scale assumptions like negligible ground effect and disc drag no longer valid. This model also accounts for the THOR's unique separated cyclic and control setup.

We choose a body frame coordinate system pinned to center of mass and aligned with the flight controller (x-y-z in Fig. 4) as much of the dynamic model is dependent on air flow velocities relative to the body frame. The 6DOF rigid body equations of motion is thus given by Eqs. (2) and (3).

$$m\dot{\boldsymbol{v}} = \sum \boldsymbol{F} - \boldsymbol{\omega} \times m\boldsymbol{v}, \tag{2}$$

$$I\dot{\boldsymbol{\omega}} = \sum \boldsymbol{\tau} - \boldsymbol{\omega} \times \boldsymbol{I}\boldsymbol{\omega}, \tag{3}$$

where m is mass, $\boldsymbol{I}$ is the moment of inertia tensor, $\boldsymbol{v}$ is the translational velocity vector and $\boldsymbol{\omega}$ is the angular velocity vector. Our objective here is to accurately determine the

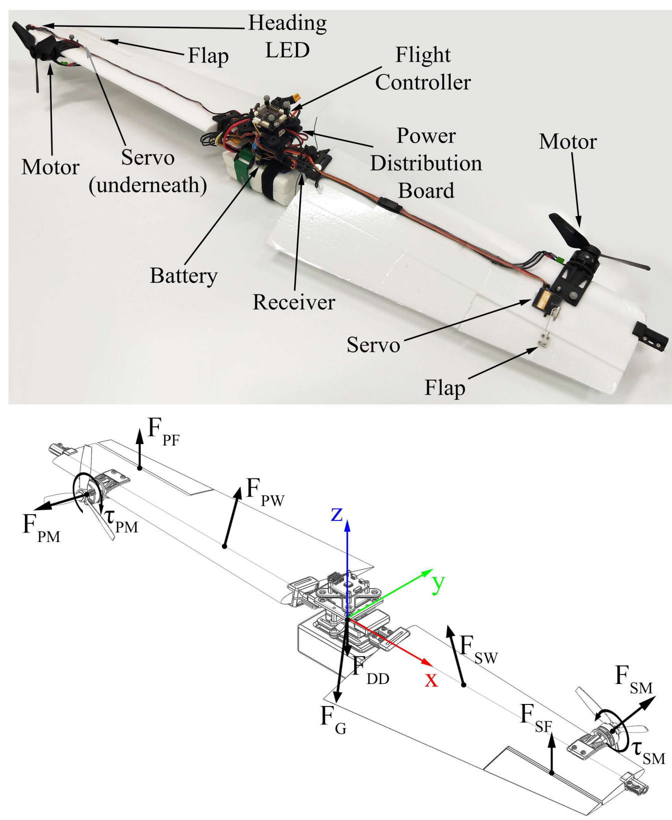

Fig. 4. THOR-Spartan prototype (above) and dynamic model (below).

components within $\sum \boldsymbol{F}$ and $\sum \boldsymbol{\tau}$, which are the body frame forces and torques, respectively.

To determine the dynamic model of the monocopter, we developed a first prototype without a transformation mechanism. This allows us to tackle the monocopter component of the design independent from the complexities of multi-mode actuation. We call this the THOR-Spartan (Fig. 4).

Named for its austere design, the wing of this prototype is locked at 0.262 radians for standardization, and ensures that the angle of attack of both wings in hover is within the optimal range for the generation of lift. For its brains, we use a custom flight controller based on the PX4 flight stack, which we currently run via a PixRacer. We also implement four additional design parameters along with some corresponding assumptions.

We use a wing design with a quarter chord length that is collinear to the x-axis from wing root to wing tip. This will allow us to assume negligible aerodynamic moment in Sec. 2.4 though it should be noted that with the exception of high speeds in forward flight, the rotational symmetry of the monocopter mode would cause the aerodynamic moments to cancel out as the freestream velocity (the total velocity of the air relative to a specified point on the craft due to external, induced, linear and angular velocity components) profile across both wings would be identical. Given that the intentions of this flight mode, we assume high forward flight speeds are not an immediate priority.

We choose to stack the flight controller, power distribution board and battery along the z-axis and as close to center of mass as possible. This is because given the lack of a tail, we expect the fixed wing configuration to be unstable unless the center of mass is close to or at the aerodynamic center of the wings (which is the quarter-chord line mentioned earlier).

We place the propulsion systems and flaps as close to the wing tips as possible. This helps us in two ways. Firstly, it alters the inertia tensor for better passive stability just like the rotational symmetry parameter mentioned earlier (More on this in Sec. 2.2). Secondly, it allows for small changes in actuation to have a large impact on net torque given the greater moment arm and faster airflow at the tip. The latter is also increased by airflow pushed through the propulsion system. The reduced actuator action also allows us to assume negligible changes to the inertia tensor during altitude, pitch and roll control (Sec. 2.4).

Lastly, we place a light-emitting diode (LED) at one of the wing tips that illuminates whenever it passes magnetic north (detected via on-board magnetometers). This is to aid debugging by providing an instantaneous notification of the craft's heading in flight.

With these parameters and assumptions, we find that we can model the forces and torques on the body frame to come from three sources (illustrated in Fig. 4)

- Mass: $\boldsymbol{F_G}$
- Propulsion Systems: $\boldsymbol{F}_{\mathrm{PM}}$, $\boldsymbol{F}_{\mathrm{SM}}$, $\boldsymbol{\tau}_{\mathrm{PM}}$, $\boldsymbol{\tau}_{\mathrm{SM}}$
- Aerodynamic Surfaces: $\boldsymbol{F}_{\mathrm{PW}}$, $\boldsymbol{F}_{\mathrm{SW}}$, $\boldsymbol{F}_{\mathrm{PF}}$, $\boldsymbol{F}_{\mathrm{SF}}$, $\boldsymbol{F}_{\mathrm{DD}}$

Note that subscript P corresponds to port, subscript S corresponds to starboard, subscript M is for motor, subscript W is for wing, subscript F is for flap and subscript DD is for disc drag.

2.2. *Mass contribution*

Mass contributes to three components of Eqs. (2) and (3); m, $\boldsymbol{F_G}$ and $\boldsymbol{I}$. As is the case with any aircraft, we would want m (and by extension the force due to gravity, $\boldsymbol{F_G}$) to be low. However, given the rotating nature of the craft, the greatest area of concern is the inertia tensor term, $\boldsymbol{I}$. Using the Intermediate Axis Theorem (also known as the Dzhanibekov Effect) [17], we determine the form of the $\boldsymbol{I}$ term that would allow for passive stability in the monocopter mode.

Through the rotational symmetry and concentration of components along the axes of the body frame, we get an inertia tensor that is close to diagonal. This is ideal in that the forces and torques along each axis have a minimized causal impact on the other axes. Hence, we can approximate our inertia tensor to be

$$\boldsymbol{I} = \begin{bmatrix} I_{xx} & I_{xy} & I_{xz} \\ I_{yx} & I_{yy} & I_{yz} \\ I_{zx} & I_{zy} & I_{zz} \end{bmatrix} \approx \begin{bmatrix} I_{xx} & 0 & 0 \\ 0 & I_{yy} & 0 \\ 0 & 0 & I_{zz} \end{bmatrix}. \tag{4}$$

Let us now assume that $I_{zz} > I_{yy} > I_{xx}$ and the craft is attempting to hover at a fixed position via a fixed angular velocity about the z-axis (ω_z). In the absence of external perturbations (a gust of wind, flying debris, etc.), we can thus assume the summation of forces and torques to be both zero and so in this scenario, if we expand Eq. (3) via Eq. (4) we get

$$I_{xx}\dot{\omega}_x = (I_{yy} - I_{zz})\omega_y\omega_z, \tag{5}$$

$$I_{yy}\dot{\omega}_y = (I_{zz} - I_{xx})\omega_x\omega_z, \tag{6}$$

$$I_{zz}\dot{\omega}_z = (I_{xx} - I_{yy})\omega_x\omega_y. \tag{7}$$

Given the small ω_x and ω_y values but significant ω_z, we can claim the time dependence of $\dot{\omega}_z$ to be negligible, whereas would have to solve further to determine impact of $\dot{\omega}_x$ and $\dot{\omega}_y$.

Knowing that $\dot{\omega}_z \approx 0$, if we differentiate Eqs. (5) and (6) and simplify using the other, we get

$$I_{xx}\ddot{\omega}_x = (I_{yy} - I_{zz})\frac{(I_{zz} - I_{xx})}{I_{yy}}\omega_z^2\omega_x, \tag{8}$$

$$I_{yy}\ddot{\omega}_y = (I_{zz} - I_{xx})\frac{(I_{yy} - I_{zz})}{I_{xx}}\omega_z^2\omega_y. \tag{9}$$

Since $I_{zz} > I_{yy} > I_{xx}$, we can see that the angular velocity along each axis will always be the negative of its jerk

$$\ddot{\omega}_x = -K_x\omega_x, \tag{10}$$

$$\ddot{\omega}_y = -K_y\omega_y, \tag{11}$$

where K_x and K_y are positive constants. By this argument, non-zero values of ω_x and ω_y are always inherently opposed by a jerk given the above design parameters. Interestingly, this also shows that the magnitude of the jerk on the x-axis will be identical to that of the y-axis ($K_x = K_y$), regardless of the differences between I_{xx}, I_{yy} and I_{zz}.

Therefore, in response to external forces and torques that produce small perturbations in ω_x and ω_y, a design that has $I_{zz} > I_{yy} > I_{xx}$ will be passively stable in a hover — hence the concentration of components along the x-axis (like the propulsion systems and flaps placements we mentioned earlier). We use the flight experiments in Sec. 2.4 to illustrate this stability.

2.3. *Propulsion systems contribution*

We use two identical sets of plastic propellers, brushless motors and Electronic Speed Controllers (ESCs) as our propulsion systems. Their dynamic contributions can be further broken down into two components, a thrust force from the air pushed by the propellers ($\boldsymbol{F}_{\mathrm{PM}}, \boldsymbol{F}_{\mathrm{SM}}$) and a torque to fulfill the conservation of momentum requirement ($\boldsymbol{\tau}_{\mathrm{PM}}, \boldsymbol{\tau}_{\mathrm{SM}}$).

There are two interesting factors to consider when modeling the propulsion systems of the monocopter.

2.3.1. *Influence of freestream velocity*

The first is that the propulsion systems are rotating with the craft itself leading to an additional, high magnitude component to the freestream velocities across the propellers. As can be seen by rotor models like [18], this phenomena can have a significant impact on $\boldsymbol{F}_{\mathrm{PM}}, \boldsymbol{F}_{\mathrm{SM}}$.

We overcome this by locking ω_z to a fixed value regardless of the craft's location in the flight envelope (be it takeoff, landing, hover or forward flight). This is a known design solution for many conventional helicopters that brings a variety of advantages to the modeling and control of the aircraft [19, 20]. In the case of the monocopter, many of these benefits carry over (as will be seen in the later sections) and with respect to the immediate challenge of modeling our propulsion systems, it has the added advantage of simplifying the problem by keeping this additional component to the freestream velocities constant.

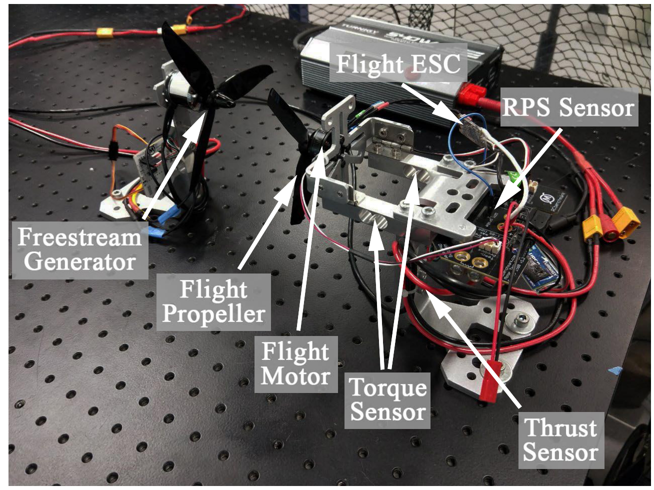

Fig. 5. Test setup to determine effects of a freestream velocity. Note anemometer is removed during testing.

The method for locking ω_z (a PI controller) is described in detail in Sec. 2.4.

Assuming that ω_z is locked, we now need to determine the magnitude of this now constant component. So, we set up a simple experiment.

As illustrated in Fig. 5 above, we mount our planned propulsion system — a 5048S Tri-Blade Propeller, DJI Snail 2305 motor and Snail 430-R ESC, on an RC Benchmark Dynamometer 1580. We generate a static equivalent of our freestream generator via another propulsion system system that pushes air towards the dynamometer from 0.15 m upstream. A power supply unit is connected to both propulsion systems to ensure a constant 12 V input and the freestream velocity near the flight propulsion system (specifically at $\frac{1}{2}$ the radius of the propeller) is measured using a hot-wire anemometer. It should be noted that when measuring the airflow across the radius of the propeller, the freestream velocity was found to be mildly turbulent but we argue that this is similar to actual flight conditions as the two propulsion systems will be flying into each other's wake when in monocopter mode.

With this setup, we take measurements of the propulsion system's rotations per second (RPS), thrust and torque across a range of simulated flight conditions (between 0–13 m/s).

From the data (Fig. 6), we can see that the freestream velocities have a noticeable relationship to thrust where the thrust force is reduced within our estimated flight conditions (10.0–13.2 m/s). That said, at any fixed freestream velocity, the force can be modeled as a linear term with respect to the command input and so

$$\boldsymbol{F}_{\mathrm{PM}} = K_{mf}u_{\mathrm{PM}}(t) + c_{mf}, \tag{12}$$

$$\boldsymbol{F}_{\mathrm{SM}} = K_{mf}u_{\mathrm{SM}}(t) + c_{mf}, \tag{13}$$

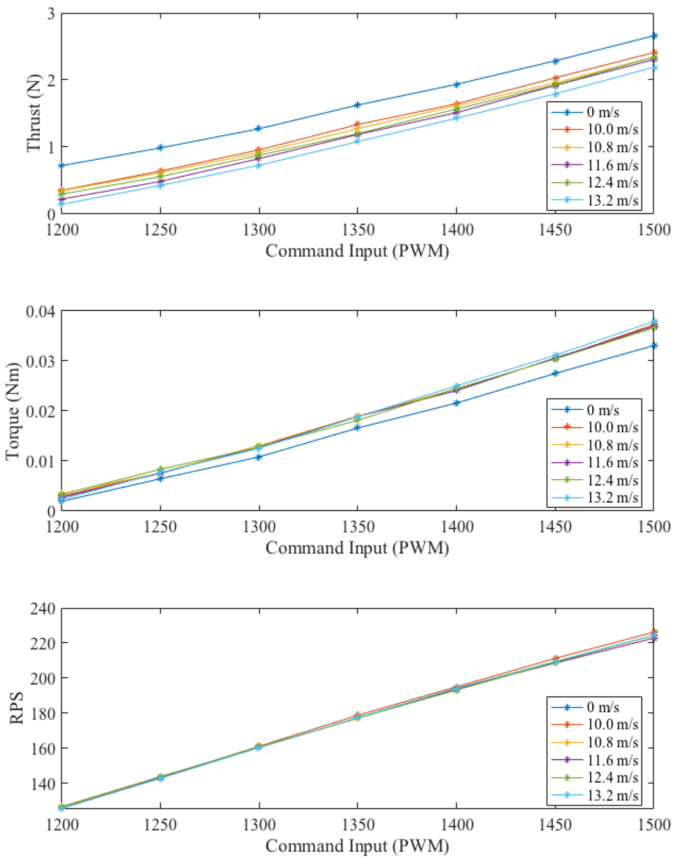

Fig. 6. Experimentally derived Thrust ($\boldsymbol{F}_{\rm SM}, \boldsymbol{F}_{\rm PM}$), Torque ($\boldsymbol{\tau}_{\rm SM}, \tau_{\rm PM}$) and RPS relationship to command input.

where K_m and c_m are the motor constants. To use these equations, we determine the hover ω_z of the monocopter mode and from there estimate the freestream velocity, thereby allowing us to choose the relevant curve on the Thrust graph in Fig. 6.

On top of informing us on its effects on thrust, the experiment also confirms a negligible effect on torque. The slight increase between 0 m/s and $\geq$ 10.0 m/s is likely due to the increased drag from the higher freestream velocities. Given its small magnitude and near identical values in the presence of non-zero freestream velocities, we can model the torque quite simply to be

$$\boldsymbol{\tau}_{\rm PM} = K_{m\tau} u_{\rm PM}(t) + c_{m\tau}, \tag{14}$$

$$\boldsymbol{\tau}_{\rm SM} = K_{m\tau} u_{\rm SM}(t) + c_{m\tau}. \tag{15}$$

Lastly, we also see a reliable relationship across the freestream velocity conditions between the pulse-width modulation (PWM) input and the propulsion system's RPS. We choose to use this to simplify our dynamic model where $u_{\rm PM}$ and $u_{\rm SM}$ are the actual PWM commands we program into the controller. This assumes a near instantaneous response between the PWM and the RPS (which is one of the reasons why we chose a race grade ESC), an assumption we feel is justifiable at this stage given the simplifications of the modeling that we seek.

It should also be acknowledged that future designs should consider using high pitch propellers since they are better suited for high freestream velocities. This would be especially worthwhile since the forward flight mode would benefit from it too. We assign this optimization to future work due to manufacturing constraints that would bring it beyond the scope of this paper's objectives.

2.3.2. *Precession torque*

The second factor is that the propulsion systems actually contribute an additional torque on top of $\boldsymbol{\tau}_{\rm PM}, \boldsymbol{\tau}_{\rm SM}$. Since ω_z is non-zero when in flight, the motors and propellers are rotating in a non-inertial frame and so a 'precession torque' needs to be accounted for. From [6], we can model it to be

$$\boldsymbol{\tau}_{\rm gyro} = \boldsymbol{I}_{\rm propulsion}(\boldsymbol{\omega}_{\rm propulsion})\boldsymbol{\omega}, \tag{16}$$

where $I_{\rm propulsion}$ is the inertia tensor of the motor, $\omega_{\rm propulsion}$ is the propulsion system angular velocity and ω is the craft angular velocity. When the propulsion system is mounted on the wing, this precession torque contributes to an increase or decrease in the angle of the wing (θ) as the torque attempts to brings the wing to an equilibrium point relative to the spinning inertia. The direction of the angle change, as Eq. (16) implies, is dependent on both the direction of rotation of the craft and the direction of rotation of the propulsion systems. For a positive increase in θ, we follow a clockwise positive convention with the thrust vector define to be the forward direction. Hence, if both the craft and its motor spins in the clockwise direction, it would have a positive increase in θ as illustrated in Fig. 7.

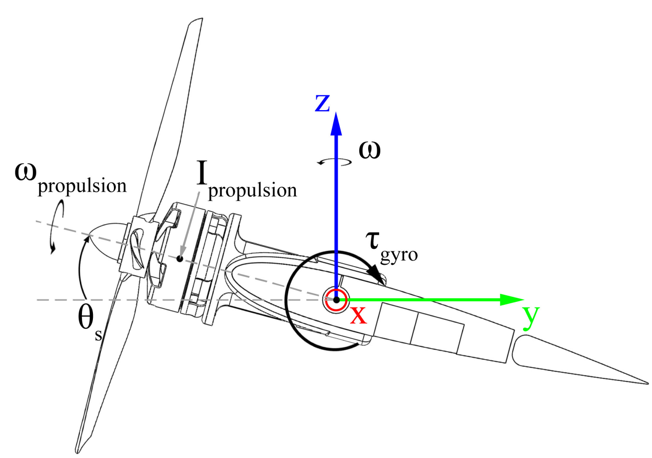

Fig. 7. Precession torque ($\boldsymbol{\tau}_{\rm gyro}$) on starboard wing. The subscript s in θ_S here is to denote the starboard wing angle.

In a single-winged, single-motored monocopter, this phenomena is accounted for by an adjustment to the starting wing angle. However, this cannot be done in a two-winged monocopter setup as, in the absence of a flexible hinge about the x-axis, an increase in θ_S would force a decrease in θ_P and vice-versa. This in turn would produce an unbalanced lift ($\boldsymbol{F}_{\text{PW}} \neq \boldsymbol{F}_{\text{SW}}$) which would critically destabilize the craft when it is attempting to hover.

We resolve this by using the second propulsion system to effect an equal but opposite torque on the craft. We modify Eq. (16) to include the second motor

$$\boldsymbol{\tau}_{\text{gyro}} = \boldsymbol{I_m}(\boldsymbol{\omega}_{\text{PM}} - \boldsymbol{\omega}_{\text{SM}})\boldsymbol{\omega}, \tag{17}$$

where ω_{PM} and ω_{SM} are the port and starboard propulsion system angular velocities respectively. Given the capabilities of the ESCs as shown in the RPS graph of Fig. 6, we are able to reliably spin both motors at near identical RPS values in identical directions, thereby negating the effects of the precession torque.

Thus, there are only specific craft-motor configurations (either both clockwise or counter-clockwise) where the torque is canceled out. We illustrate this in Table 1 below where Configurations A, D, E and H are the viable configurations. All our THOR prototypes follow Configuration A.

As a last comment on the topic of precession torque, it can be seen from Eq. (17) that if we could precisely measure and control ω_{PM} with respect to ω_{SM}, we could potentially control body frame pitch (rotation about the x-axis) while maintaining a constant ω. This could be useful for stabilizing or even controlling the pitch/roll of the craft without having to engage any flaps. We leave this unique potential for a dual-wing monocopter to be the focus of a future work.

2.4. *Aerodynamics contribution*

Aerodynamics is a complex phenomenon and it often relies on a more empirical rather theoretical solution, thus necessitating a slightly different approach compared to our two previous subsections. As with many other aerial systems, we start our aerodynamic model with the Blade Element Theory (BET)

$$d\boldsymbol{L} = \frac{1}{2}\rho c C_l U^2 dx, \tag{18}$$

$$d\boldsymbol{D} = \frac{1}{2}\rho c C_d U^2 dx, \tag{19}$$

where $d\boldsymbol{L}$ and $d\boldsymbol{D}$ are the incremental lift and drag forces per unit span dx, ρ is the density of air, c is the local blade chord length, C_d is the drag coefficients and U is the free-stream velocity at the blade element (illustrated in Fig. 8). Summing up the incremental terms across a wing (where subscript n denotes the nth blade for a total of at least 40 blades [19]), we get the total lift $\boldsymbol{L}$ and total drag $\boldsymbol{D}$ vector for each wing, which we combine to form the aerodynamic force ($\boldsymbol{F}_{\text{PW}}$ for port wing and $\boldsymbol{F}_{\text{SW}}$ for starboard wing). Note that $d\boldsymbol{L}$ and $d\boldsymbol{D}$ are defined to act perpendicular and parallel to the vector U, respectively (also in Fig. 8).

For rotor wings, the BET is usually combined with Momentum Theory to form the Blade Element Momentum Theory (BEMT). This allows for the modeling of the downward airflow that is induced by the rotor action. Similarly, additional model components of varying complexity are then added to account for the various regions of the flight envelope- forward flight, ground effect, high altitude to name a few. Combined, these make for a highly accurate but computationally intensive model. For the insights that we seek, a simpler model would suffice in exchange for lower costs and faster development times.

Table 1. Rotation configurations.

Config.	Craft rotation (ω)	Port motor (ω_{PM})	Starboard motor (ω_{SM})	Precession effect (τ_{gyro})
A	+	+	+	0
B	+	+	−	+
C	+	−	+	−
D	+	−	−	0
E	−	+	+	0
F	−	+	−	−
G	−	−	+	+
H	−	−	−	0

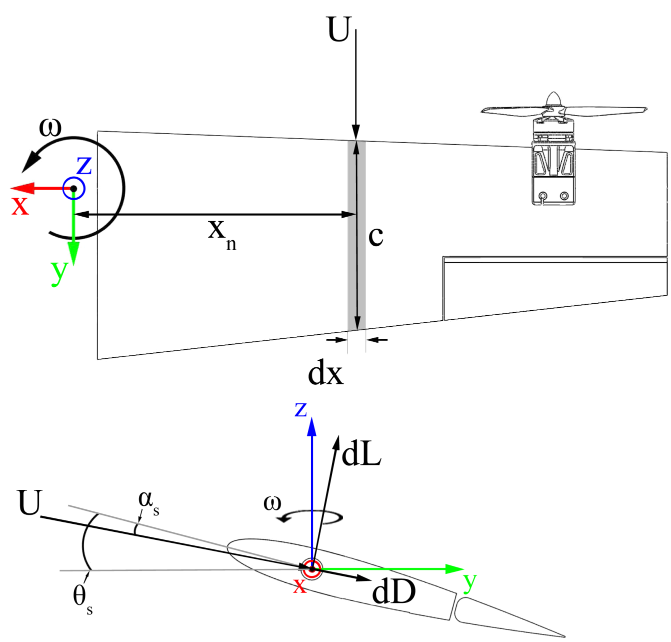

Fig. 8. Basic aerodynamic variables.

As much as possible, we would also like this model to rely only on on-board measurable states, thereby allowing us to design a controller that would work outside of highly controlled environments.

To this end, we take a cascaded approach to determining our aerodynamic forces. We first model the wing's drag component. From there we implement the fixed ω_z controller we mentioned earlier, which provides the benefit of keeping several of our aerodynamics assumptions valid. We then model the wing's lift with which we combine with the drag component to determine F_{PW} and F_{SW}. With these we determine any remaining vertical contributors to the aerodynamic forces. In the case of the THOR, we determined these to be disc drag ($\boldsymbol{F}_{\mathrm{DD}}$) and ground effect. Finally, we wrap up the aerodynamic model with the flap components ($\boldsymbol{F}_{\mathrm{PF}}$ and $\boldsymbol{F}_{\mathrm{SF}}$).

2.4.1. *Wing drag*

We chose to tackle the drag term first for several reasons. Firstly, it will give us insight on ω_z as it produces the dominant counteracting torque to the torque produced by the propulsion system's thrust. Secondly, we suspect that the drag term is the most independent of the aerodynamic forces and torques as its primary contributor is the high magnitude ω_z. Lastly, it is the easiest to measure given that ω_z can be measured via the on-board magnetometer and gyroscope.

We start by using the BET model to describe torque and so Eq. (19) gives

$$d\boldsymbol{\tau_D} = x_n\left(\frac{1}{2}\rho c C_d U^2 dx\right), \tag{20}$$

where $d\boldsymbol{\tau_D}$ is the elemental torque component and x_n is the x-axis distance of the nth blade element. Summing up the element torques across each wing will give the total torque due to drag $\boldsymbol{\tau_D}$.

Given a nonchanging wing, we can simplify a lot of components in $\boldsymbol{\tau_D}$. The x_n component when summed up would be a constant. ρ can be assumed to be constant as changes to local temperature and humidity would be negligible in hovering flight. c is a function of x, thus making it also a constant. C_d remains as a variable, being a function of the angle of attack (α_p and α_s). Lastly, U can be simplified into its primary component, $x_n\omega_z$, which we can separate.

As such, our total drag torque per wing can be given by

$$\boldsymbol{\tau_D} = k_{wd} C_d(\alpha)\omega^2. \tag{21}$$

Given the fixed wing angle of the THOR-Spartan, for the purpose of determining k_{wd}, we can set C_d to be a constant for now (which we determined via the open source airfoil analysis tool, XFLR5).

To determine k_{wd}, we implement a PI controller on both the propulsion systems and so $u_{\mathrm{PM}}(t)$ and $u_{\mathrm{SM}}(t)$ (in Eqs. (12) and (13), respectively) obey the following control law:

$$u(t) = K_p e(t) + K_i \int_0^t e(\omega_z) d\omega_z, \tag{22}$$

where K_p and K_i are the proportional and integral gains, respectively, and e is the angular velocity error.

We manually tune the gains and then conduct a flight test where we vary the desired ω_z value. We chose a range of values between 28 rad/s and 33 rad/s, which we believe is the region where the craft would be able to achieve hovering flight. On the craft, we record both the ω_z measured by the craft's magnetometer and gyroscope and the PWM commands sent to the two motors (u_{PM} and u_{SM}). To verify the ω_z, we also record it externally using motion capture cameras as shown in Fig. 9.

Feeding the u_{PM} and u_{SM} commands into a simulation that uses the model defined by Eq. (21), we determine a value for k_{wd} by finding a value that gives the global minimum root-mean-square error (RMSE) for ω_z. For THOR-Spartan, we determine this to be $k_{wd} = 0.0079$, whereby the simulation and actual result for ω_z compares as shown in Fig. 10.

The coefficient remained constant for successive flight tests with the PI controller for ω_z proving itself to be sufficiently reliable for us to proceed to modeling the next aerodynamic component, wing lift.

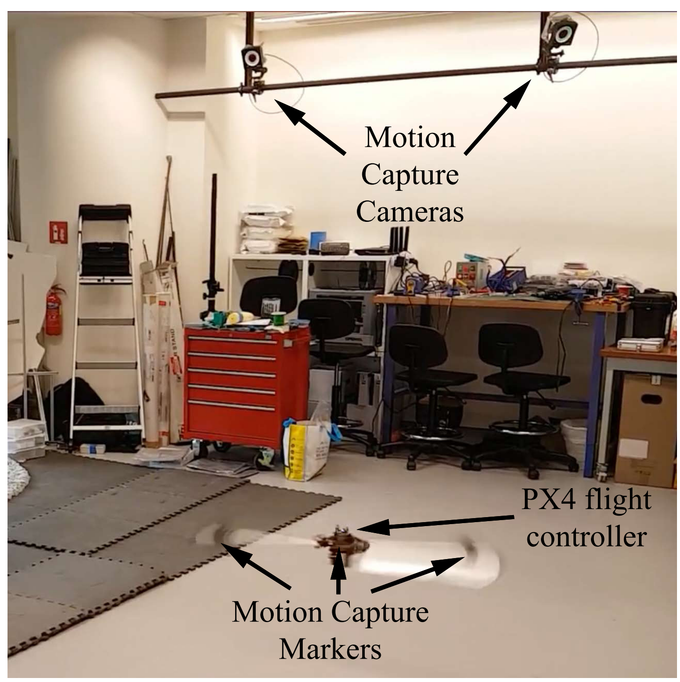

Fig. 9. Wing Drag flight test setup.

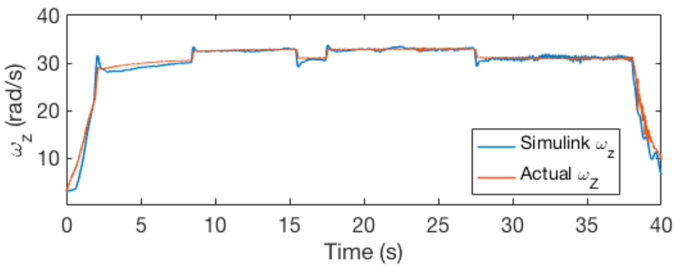

Fig. 10. Comparison of simulation and actual ω_z.

2.4.2. *Wing lift*

Using the same process as we did for the drag term, we use a varying ω_z to determine an estimate of a simplified lift term.

For the same reasons we gave for Eq. (20) (sans the constant $\sum x_n$ term as this is a force and not a torque), we can simplify Eq. (18) to get

$$\boldsymbol{L} = k_{wl} C_l(\alpha)\omega^2. \tag{23}$$

For wing lift, we verify the dynamics using measurements of the body-frame vertical velocity (vel$_z$). While we draw our velocity data from both the flight controller and motion capture setup, it should be noted that the position data that we will present below is exclusively from the Optitrack. This is because the default altitude sensor on our flight controller, a barometer, is inaccurate for the small range of altitudes we are interested in (0–2 m). Future versions of the THOR would include a Time-of-Flight (ToF) sensor so as to bring us one step closer to our goal of using on-board only measurements.

However, when we attempt to choose the coefficient with the lowest RMSE across the flight time, we not only get an extremely low lift coefficient (one order of magnitude lower than expected), we also get an absurdly inaccurate simulation equivalent (Base Model in Fig. 11).

We attempted to reduce the inaccuracy by also accounting for additional drag via vertical freestream during rotor action using the component

$$\boldsymbol{F}_{\mathrm{DD}} = k_{\mathrm{dd}}(\mathrm{vel}_z)^2. \tag{24}$$

where k_{dd} is the disc drag coefficient and vel$_z$ is the vertical velocity of the craft. But even with this factored in, the simulation plots were inaccurate. However, it did reveal that the missing component had some correlation with altitude. In fact, we observed from our flight tests that at every step increase in ω_z, the craft would briefly climb before reaching an equilibrium world frame Z position (Pos$_z$). We thus suspected that our aerodynamic lift model required the inclusion of a ground effect component.

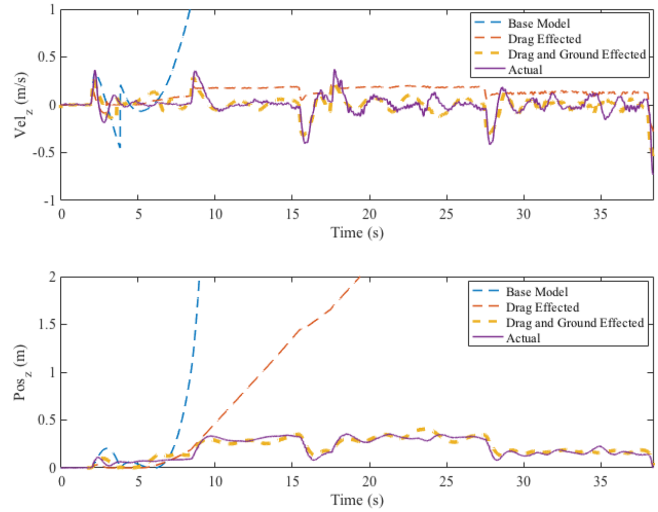

Fig. 11. Comparison of simulated and actual Vel$_z$ and Pos$_z$.

To include the ground effect, we use the simplified consideration from [19]

$$\frac{\boldsymbol{T}}{\boldsymbol{T}_\infty} = \begin{cases} \dfrac{1}{1-\frac{R}{4z}^2}, & \text{for } \dfrac{z}{R} \geq 0.5 \\ c_{ge}, & \text{otherwise,} \end{cases} \tag{25}$$

where T is the combined aerodynamic lift of both the wings after accounting for ground effect, T_∞ is the combined aerodynamic lift of both the wings given by Eq. (23) (which by itself does not account for ground effect), R is the wing radius and z is the world frame height. We set an otherwise condition for $\frac{z}{R} \geq 0.5$ to avoid having an infinite lift condition at take-off and landing.

Using an RMSE, we determine the optimal combination of k_{wl}, c_{ge} and k_{dd} (we ensure the combination is valid by using the theoretical values as the starting point). With $k_{wl} = 0.00170$, $c_{ge} = 0.15$ and $k_{\mathrm{dd}} = 3.889$, we get the 'Drag and Ground Effected' plot in Fig. 11, which is the closest of all the models thus far.

This ground effect factor is not usually modeled, having only a brief mention in [6] and no mention in other single-motored, single-winged monocopter papers. This is likely due to the relatively small sizes these prototypes, where the R term in (25) is relatively small, allowing its contribution to be assumed as negligible. Given the larger size of the THOR prototypes, the potentially long flight times near the ground and the simple but high impact contribution of a ground effect model, we feel that Eq. (25) is worth keeping in our dynamic model.

2.4.3. *Flap component*

We reach the final two components of our model $\boldsymbol{F}_{\mathrm{PF}}$ and $\boldsymbol{F}_{\mathrm{SF}}$. Given their position close to the wing tips, the blade elements here have a long moment arm with respect to any small oscillations of ω_x and ω_y and the hovering ω_z. This makes modeling of the freestream velocities (U) in this region difficult. To make matters worse, we observed that the craft experiences small amounts of precession during hovering flight due to the small but non-zero products of inertia and the slightly angled motors. This in turn contributes to a tendency for the craft to enter into an increasing spiral over long durations of uncorrected hover or when exposed to repeated perturbations about the x- and y-axes, which in turn add additional components to the U term.

The difficulties of modeling U for the development of a controller is mostly a sensing problem. The ability of the on-board inertial-measurement unit (IMU), which in our case comprises of gyroscopes, magnetometers, accelerometers and barometers, to sense wing attitude and velocities still falls short of their helicopter equivalent- the swashplate. This is understandable as the swashplate essentially provides a mechanical calculation with the control input built-in, thus giving it an unparalleled response time and precision.

And neither is the IMU entirely useless. Our objective is insight and current off-the-shelf IMUs, in combination with robust filters and fusion algorithms, are sufficient for this capacity. While simulation and actual results differ due to unpredictable and often diverging instantaneous values of U, we were able to observe that a P controller is sufficient for a pilot to hold his/her position within a 1.5 m by 1.5 m grid indefinitely, as shown by Fig. 12 below, which we measured via our motion capture setup.

As an interim to a more complete model, we can also attempt to determine the relationship between pilot input to F_{PF} and F_{SF} by using the flaps as a collective input. While the intended control of the THOR would be to use slow but high torqued servos for a collective input onto the wing and fast but low torqued servos for cyclic control (at the flaps), we could temporarily use the flaps for collective control and determine their lift component from changes in vel_z and their drag component from changes in ω_z.

We use the following model for the flaps:

$$\boldsymbol{L}_{\text{flap}} = k_{\text{fl}} C_{l\delta} u_\delta(t)\omega^2, \quad -\frac{\pi}{8} \le u_\delta \le \frac{\pi}{8}, \tag{26}$$

$$\boldsymbol{D}_{\text{flap}} = k_{\text{fd}} C_{d\delta} u_\delta(t)\omega^2, \quad -\frac{\pi}{8} \le u_\delta \le \frac{\pi}{8}, \tag{27}$$

where k_{fl} and k_{fd} are the flap lift and drag constants, $C_{l\delta}$ and $C_{d\delta}$ are our lift and drag gradients and $u_\delta(t)$ is our command inputs. Note that we can assume the lift and drag gradients are linear because we operate at small values of u_δ.

We conduct a flight test where we fly the craft at various target ω_z (0–25 s in Fig. 13) but also with an added flap control in the form of a collective input (25–75 s in Fig. 13). At $k_{\text{fl}} = 2.586 \times 10^{-5}$ and $k_{\text{fd}} = 1.850 \times 10^{-5}$ we get a sufficiently accurate model of the flaps close to equilibrium conditions, as shown in Fig. 13.

Note that in this model, we use small perturbations to the roll of the craft to induce forward flight in any direction of our choice. The flaps induce these roles through a timed cyclic output across each period of rotation of the craft. We keep the command inputs small so as to keep the model within the assumptions of small rotational perturbations about the x- and y-axes and a low forward flight speed.

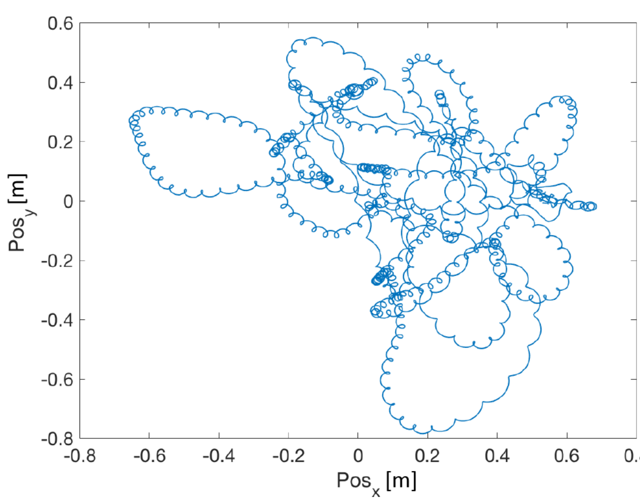

Fig. 12. Pos_x and Pos_y translation during a 70 s hover. Note the curls due to mild precession and nutation.

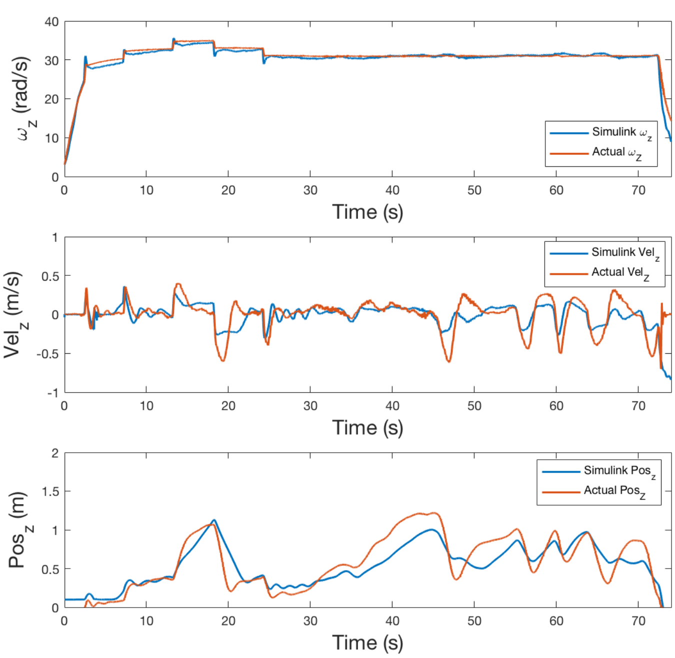

Fig. 13. Comparison of simulation to actual dynamics over a minute long flight.

With this flap component accounted for, we complete the monocopter model of the THOR. A summary of the configuration used for the experiments can be found in Table A.1 in Appendix A.

3. Flight Transition

Given the THOR's similarity to tailsitter based fixed-wings, our remaining hurdle is the transition step. Of the two directions, hover to cruise and cruise to hover, we decide to focus on the FT (hover to cruise) for this publication as this transition is harder to achieve due to the rotating nature of the hovering mode.

To simplify the problem, we separate the FT sequence into two phases, FT-a and FT-b. FT-a encompasses the phase where the rotational motion of the craft is reduced to a halt, and FT-b involves the reorientation of the craft to the fixed wing configuration.

3.1. *Transition dynamic model*

Unlike the hovering mode where the wing angles stay at reasonably small values (like the fixed 0.262 rad for the THOR-Spartan), the transition sequence requires the craft to go into states where the wing angles reach $\frac{\pi}{2}$ radians. Due to this larger operating range, a simpler dynamic model specific to this transition sequence is utilized. To explore this model, we built on our findings from the THOR-Spartan and developed a second prototype, the THOR-Mini that also includes a high torque, low speed servos for collective control and the transition step.

3.1.1. *Free body diagram*

In addition to the existing body frame (x-y-z), we now add an inertial frame (X-Y-Z). It is important to note that in the cruising mode, the body frame z-axis is now the roll axis and the body frame x-axis is now the pitch axis, where the positive x-axis is now pointing to the starboard of the craft. An illustration of these free body diagram components with respect to the THOR-Mini is shown in Figs. 14 and 15.

$$\sum \boldsymbol{F}_{\text{thor}} = \boldsymbol{F}_P + \boldsymbol{F}_S + \boldsymbol{A}_{\text{PW}} + \boldsymbol{A}_{\text{SW}} + \boldsymbol{W}, \tag{28}$$

$$\begin{aligned}\boldsymbol{\tau}_{\text{thor}} = {} & \boldsymbol{\tau}_P + \boldsymbol{\tau}_S + \boldsymbol{\tau}_{\text{PW}} + \boldsymbol{\tau}_{\text{SW}} + (\boldsymbol{r}_{pm}) \times \boldsymbol{F}_P \\ & + (\boldsymbol{r}_{sm}) \times \boldsymbol{F}_S + (\boldsymbol{r}_{pw}) \times \boldsymbol{A}_{\text{PW}} + (\boldsymbol{r}_{sw}) \times \boldsymbol{A}_{\text{SW}}\end{aligned} \tag{29}$$

While the craft is governed by the same 6DOF equations of motion described in Eqs. (2) and (3), we chose to divide our forces in a slightly different manner. $\boldsymbol{F}_P$ and $\boldsymbol{F}_S$ are motor thrust forces, $\boldsymbol{A}_{\text{PW}}$ and $\boldsymbol{A}_{\text{SW}}$ are the total aerodynamic forces acting on each wing, which comprises of the lift and drag forces, such that $\boldsymbol{A}_{\text{PW}} = \boldsymbol{L}_P + \boldsymbol{D}_P$ and $\boldsymbol{A}_{\text{SW}} = \boldsymbol{L}_S + \boldsymbol{D}_S$. $\boldsymbol{\tau}_P$ and $\boldsymbol{\tau}_S$ are torques caused by the motors. $\boldsymbol{\tau}_{\text{PW}}$ and $\boldsymbol{\tau}_{\text{SW}}$ refer to the aerodynamic torques.

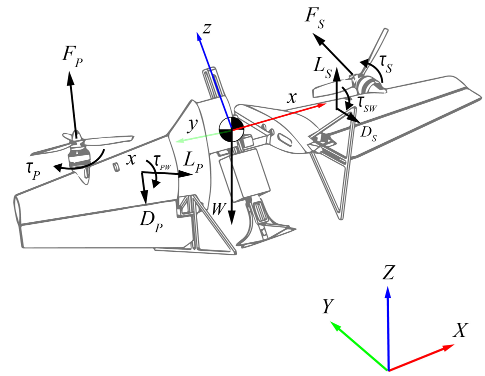

Fig. 14. Free body diagram of the THOR-Mini during the transition phase.

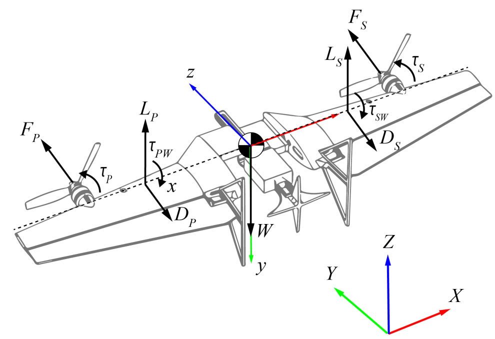

Fig. 15. Free body diagram of the THOR-Mini in fixed wing configuration (cruising mode).

Torques caused by the motor and aerodynamic forces for each wing are also included in the torque equation. $\boldsymbol{r}_{\text{PM}}$ and $\boldsymbol{r}_{\text{SM}}$ denote the positions of the motors, $\boldsymbol{r}_{\text{PW}}$ and $\boldsymbol{r}_{\text{SW}}$ denote the positions of the aerodynamic reference points, with respect to the body frame center of mass.

3.1.2. *Aerodynamic forces and moments*

Just like in the monocopter model, we use a modified BET model in place of a BEMT model to determine the lift generated by the wings. This simplifies the calculations and gives validity over a wider operating range of wing angles. In fact, the formulation used here is similar to works involving the dynamics of tailsitters such as [21, 22]. Other aerodynamic assumptions specific to our transition step are defined as follows:

- Flow is assumed to be uniform throughout the wing despite the UAV being in rotation at the start of the transition sequence.

- The entire wing is taken to be inside the propeller slipstream.
- Sideslip effects are ignored.
- Forces and moments are independently calculated for each wing with no coupling effects.

A local coordinate system for the wing is defined at the aerodynamic reference point as $[x_w, y_w, z_w]$, with x_w pointing toward the leading edge and y_w pointing upwards. The propeller spin induces a flow in the negative z_w direction on the wings, and the total magnitude of the flow in this axis can be approximated using Momentum Theory [20]

$$v_{\mathrm{sum},z_w} = \sqrt{v_{z_w}^2 + \frac{2F_{\mathrm{prop}}}{\rho_{\mathrm{air}} A_{\mathrm{prop}}}}. \tag{30}$$

From the x_w and y_w components of the velocity, we can deduce both the incident angle and the magnitude of the total freestream velocity, V_∞

$$\alpha = \mathrm{atan2}(v_{y_w}, v_{\mathrm{sum},z_w}), \tag{31}$$

$$V_\infty = \sqrt{v_{y_w}^2 + v_{\mathrm{sum},z_w}^2}. \tag{32}$$

The lift forces, drag forces and torques acting on the wing can thus be deduced using the equations below (where C_l, C_d and C_m are functions)

$$L = qC_l(\alpha, \delta)S, \tag{33}$$

$$D = qC_d(\alpha, \delta)S, \tag{34}$$

$$M = qC_m(\alpha, \delta)S, \tag{35}$$

where q is the dynamic pressure, $q = \frac{1}{2}\rho U^2$. Functions C_l, C_d and C_m can be expanded into the following equations:

$$C_l(\alpha, \delta) = c_l(\alpha) + c_{l_\delta}\delta, \tag{36}$$

$$C_d(\alpha, \delta) = c_d(\alpha) + c_{d_\delta}\delta, \tag{37}$$

$$C_m(\alpha, \delta) = c_m(\alpha) + c_{m_\delta}\delta. \tag{38}$$

c_{l_δ}, c_{d_δ}, and c_{m_δ} are coefficients describing the first-order effects of wing flap deflection which is dependent on the craft's geometry.

Functions $c_l(\alpha)$ and $c_d(\alpha)$ are airfoil section data obtained experimentally from $0 \le \alpha \le \frac{\pi}{2}$ radians [23].

The forces and torques acting on the body frame due to F_{wing} is expressed as follows:

$$\boldsymbol{F}_{\mathrm{aero,body}} = R_{w,b}(\theta)\boldsymbol{F}_{\mathrm{wing}}, \tag{39}$$

$$\boldsymbol{\tau}_{\mathrm{aero,body}} = \boldsymbol{r}_{\mathrm{wing}} \times \boldsymbol{F}_{\mathrm{aero,body}}, \tag{40}$$

where $R_{w,b}(\theta)$ is the 2D rotation transformation by angle θ, which is the angle between the frames (x'_w, y'_w) and (x_w, y_w). $\boldsymbol{r}_{\mathrm{wing}}$ is a translation vector from the body reference frame to the wing reference point.

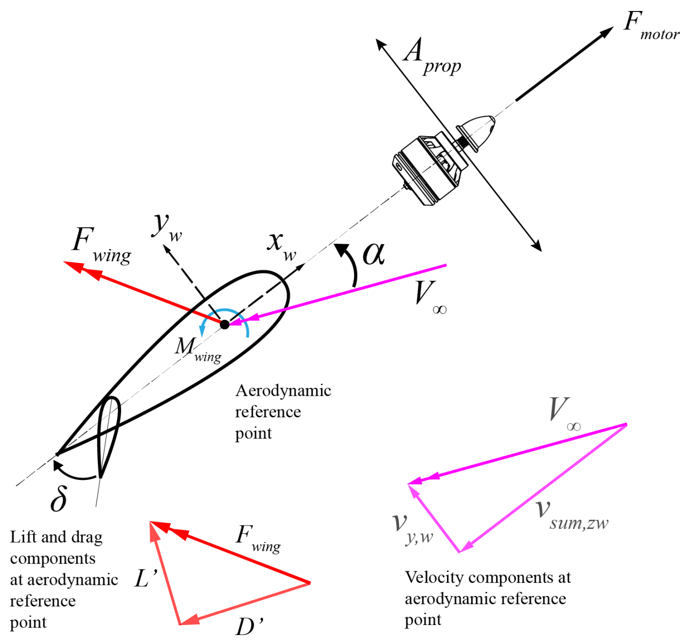

Fig. 16. Illustration of aerodynamic forces and torques overlaid on a 2D-Section View of the Wing.

3.2. *Forward transition (FT-a)*

The objective of this phase would be to reduce the rotational motion of the craft to a halt in preparation for the next phase of the full transition sequence. It is also during this phase where the wings physically rotate into the cruising mode configuration.

The controller to be used for this phase is a cascaded attitude-rate controller typically used in multi-rotors [24]. Attitude commands are fed through the attitude controller which outputs rate commands. Rate commands are directly processed by the rate controller into actuator commands. A simplified control diagram is shown in Fig. 17.

The controller is already natively implemented within the open-source PX4 Flight Stack. More details of the controller and implementation can be found in [24, 25].

For the duration of the FT-a phase, a desired attitude for pitch and roll is set such that the body z-axis coincides with the inertial Z-axis. The desired yaw rate, $\omega_{\mathrm{des},z}$ is set to be zero.

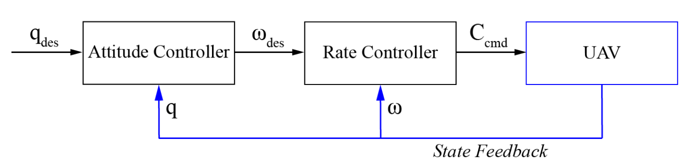

Fig. 17. Simplified control diagram of the cascaded controller.

3.3. *Forward transition* (*FT-b*)

In this phase, the craft is required to re-orientate from the hovering to a fixed wing configuration. The strategy we adopt here is similar to [21], where the craft's body rate time histories during the reorientation phase is directly obtained by trajectory optimization. It is assumed during this optimization that the body rates can be controlled directly.

3.3.1. *Optimization formulation*

$$\begin{aligned} \min_{\omega} t_f^2 + \int (1 + q_z(t)^2) \cdot \omega_x(t)^2) + \omega_y(t)^2 + \omega_z(t)^2 dt \\ \text{s.t.} \quad \dot{\boldsymbol{q}} &= \frac{1}{2}\boldsymbol{W}(\boldsymbol{q})^T\boldsymbol{\omega}, \\ \|\boldsymbol{q}\| &= 1, \quad \forall\, t, \\ \boldsymbol{q}(\boldsymbol{0}) &= \boldsymbol{q_0}, \\ \boldsymbol{q}(\boldsymbol{t_f}) &= \boldsymbol{q_f}. \end{aligned} \tag{41}$$

The objective function to be minimized includes both an endpoint term and integral terms. The endpoint term, t_f^2, seeks to minimize the time taken for the craft to re-orientate to the fixed wing configuration. The body rates are penalized quadratically for each axis. The weighting term on $\omega_x(t)$, $1 + q_z(t)^2$, increases with yaw deviation to decrease the reliance on pitch actuation as the yaw deviation increases. No weighting terms are imposed on $\omega_y(t)$ and $\omega_z(t)$.

The optimization is also subject to the dynamics constraint described by the quaternion rate equation, $\dot{\boldsymbol{q}} = \frac{1}{2}\boldsymbol{W}(\boldsymbol{q})^T\boldsymbol{\omega}$, where $\boldsymbol{W}(\boldsymbol{q})$ is the quaternion rate matrix [26]:

$$\boldsymbol{W}(\boldsymbol{q}) = \begin{bmatrix} -q_x & q_w & q_z & -q_y \\ -q_y & -q_z & q_w & q_x \\ -q_z & q_y & -q_x & q_w \end{bmatrix}. \tag{42}$$

Due to the parameterization of the quaternion as $\boldsymbol{q} \in \mathbb{R}^4$, a norm constraint has to be imposed on the quaternion vector, $\boldsymbol{q}$, to ensure a valid rotation representation at all times.

3.3.2. *Optimization results*

The optimization routine was run for varying initial yaw headings within the range $[0, \pi]$ to obtain a set of trajectories. Appropriate symmetry transformations were used to derive trajectories for $[-\pi, 0]$.

The results are collapsed into a lookup table for the body rates of each axis that can be expressed as, $w_{i,\text{des}} = F_i(t, \text{yaw}_{\text{init}})$, where subscript i refers to the axis of interest. A 3D Delaunay triangulation with linear barycentric interpolation between the triangles is used for interpolation between the points. The lookup tables can be visualized as surface plots as displayed in Fig. 18.

As different initial yaw angles would result in different trajectory lengths, a separate 1D lookup table was defined based on the optimization results, specifically the final time t_f of the trajectories. Linear interpolation was used between points. A plot of the trajectory length varying with initial yaw angles is shown in Fig. 19.

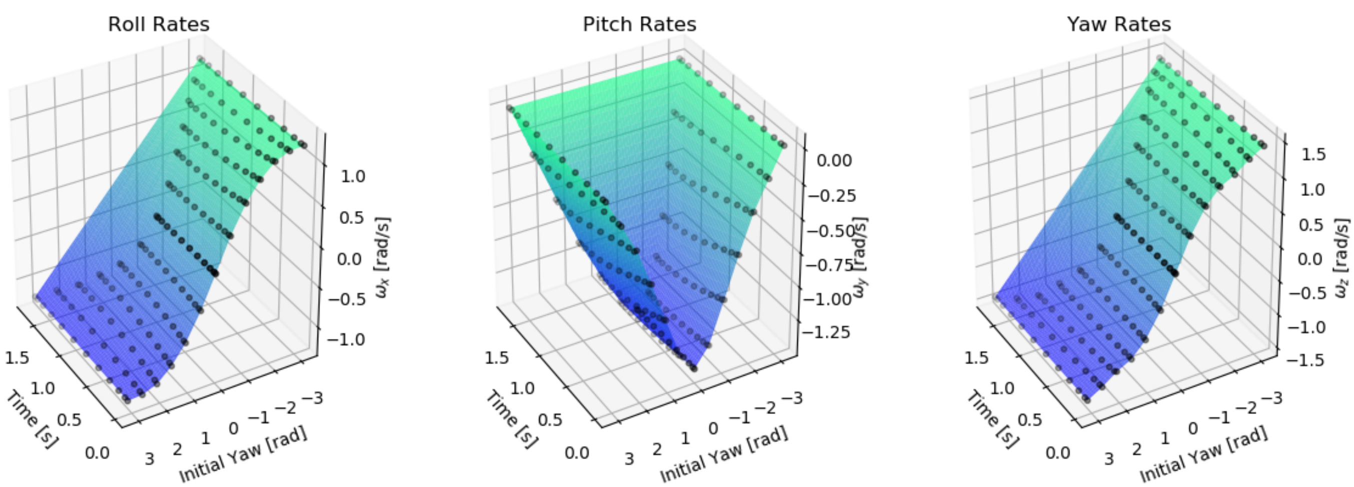

Fig. 18. Interpolated surface plots of body rates against initial yaw and transition time. The black points represent the discretized trajectories obtained from the optimization routine.

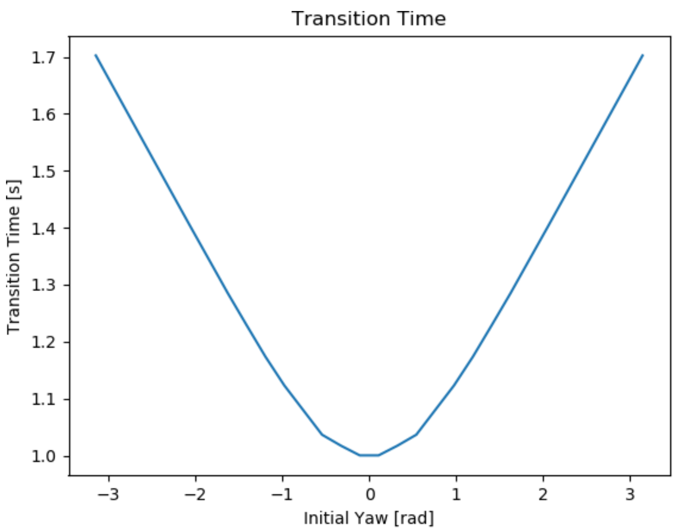

Fig. 19. Plot of the transition length against initial yaw.

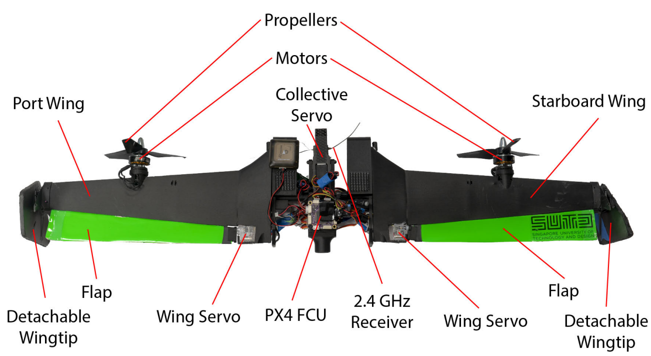

Fig. 20. THOR-Mini prototype

3.4. *Experimental results*

To validate the performance of our FT strategy, real-world transition tests were carried out using the THOR-Mini within our motion capture environment.

3.4.1. *Experimental setup*

Given the different testing objectives of the THOR-Mini, it is important that we acknowledge its major differences with respect to its predecessor, the THOR-Spartan

- A high torque, low speed collective control mechanism that is also used for the transition step.
- Smaller wingspan due to limited space for transition in motion capture environment.
- Design changes for increased crash resistance (namely carbon fiber composite wings, snap-on motors, cyclic servos and detachable wing tips)

That aside, just like in the THOR-Spartan, the prototype runs on our customized PX4 flight controller via the Pixracer. The flight controller is used for low level flight stabilization that computes actuator commands from higher level rate and angle commands. As mentioned earlier, the controller described in Sec. 3.2 is already natively implemented in the PX4 flight stack. Low level actuator commands are computed via control allocation. Rate and angle commands are sent over WiFi from an off-board computer via MAVLink packets, a lightweight protocol for UAV communication [27]. The prototype that was used for the transition experiments is shown in Fig. 20 and a summary of its configuration can be found in Table A.2 in Appendix A.

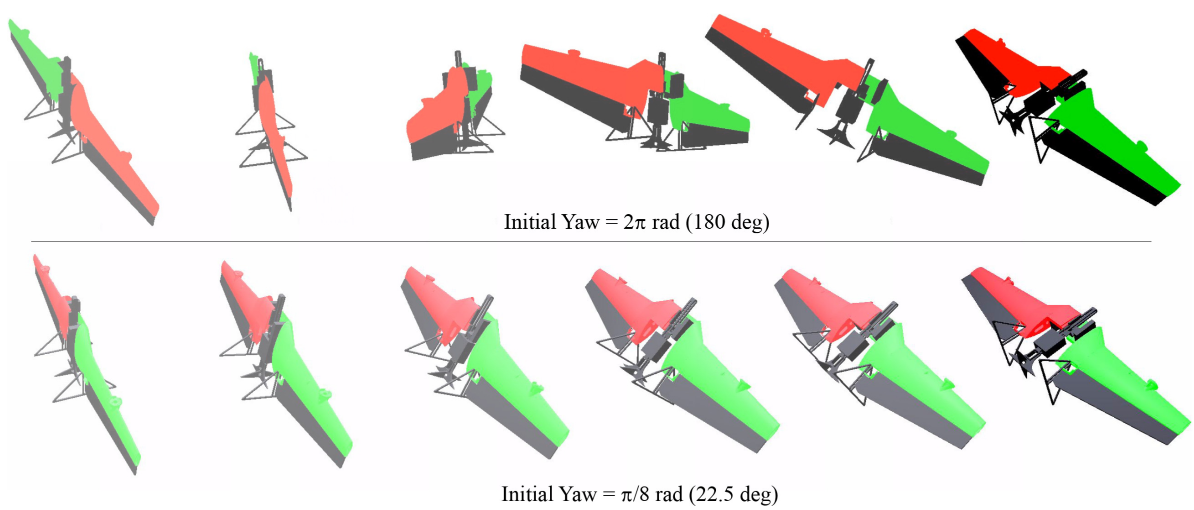

Fig. 21. From left to right: Snapshots of a FT-b trajectory (reorientation to fixed wing) with an initial yaw angle of π radians and 0.393 radians. Red denotes the port (left) side of the craft.

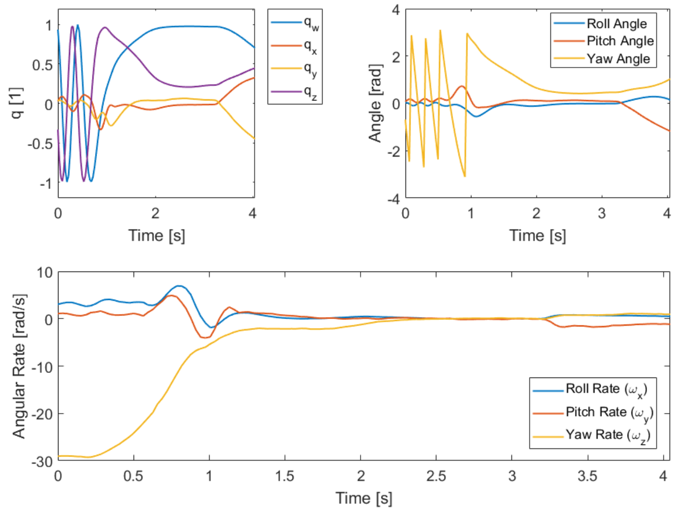

Fig. 22. Attitude time histories for the entire transition duration (FT-a + FT-b).

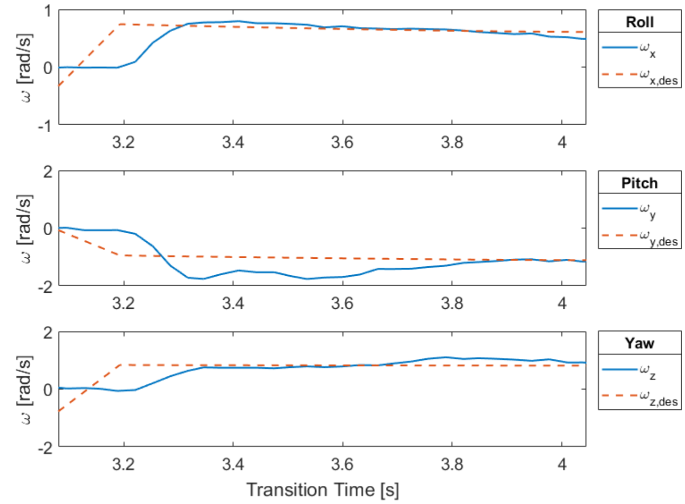

Fig. 23. Actual and target body rates during FT-b phase.

3.4.2. *Forward transition tests*

The commands to be sent to the craft are derived from the results obtained from Secs. 3.2 and 3.3. The craft is first flown in hover mode for at least 5 s, before initiating the FT sequence to cruising mode at various initial yaw conditions. An illustration of two such tests can be found in Fig. 21.

Figure 22 describes the attitude of the craft during a successful transition sequence for phases FT-a and FT-b. Figure 23 shows the comparison between the desired body rates and the actual body rates during the second phase of the transition sequence (FT-b). For this particular flight, the target final yaw was set to $\pi/2$ radians (toward East, 0 rad yaw angle corresponds to magnetic north). 0 s corresponds to the initiation of the transition sequence.

From the first 2 s of the transition sequence, the halting of the rotation can be deduced from the yaw rate as seen in Fig. 22. As shown in the 3–4 s region in the angle graph of Fig. 22, the pitch angle can be seen approaching $-\pi/2$ as it transits towards cruising mode by pitching forward. The yaw angle also approaches the yaw end target of $\pi/2$. The sawtooth nature of the yaw angle is due to the property of Euler angle representation possessing a discontinuity at π radians. (The peaks of the displayed graph do not hit π and $-\pi$ all the time due to aliasing in the data capture). An image sequence depicting the successful transition can be found in Fig. 24.

3.5. *Cruising mode tests*

As a follow up to the previous subsection for the transition step, we test if the UAV is flyable in the cruising configuration. So far we have assumed it to be achievable given the THOR's similarity to a tailsitter. Using existing PX4 software, the cruising configuration was tested in an outdoor environment. Figure 25 shows a map overlay of the entire flight path on one mission where we successfully executed 3 different maneuvers in a 15,600 m^2 field.

Throughout these flight tests, we were able to keep the craft airborne at an average cruising speed of 7.9 m/s (max 17.2 m/s) at about 8 m above ground while also using about 25% less throttle than if we were to attempt to maintain a stationary hover as a tailsitter. This implies that the wings are effectively contributing a lift force on the craft. The ground speed and altitude data for a test flight are presented in Fig. 26. It is also worth noting that due to the use

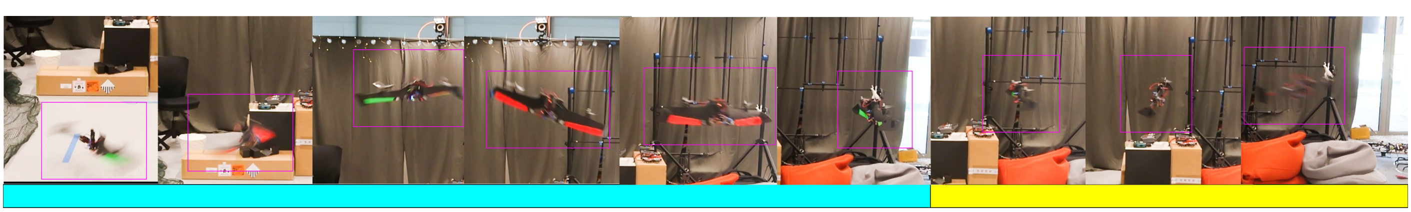

Transition Phase **FT-a**
Stopping Rotation

Transition Phase **FT-b**
Reorientate to cruising mode

Fig. 24. From left to right: Snapshots of a successful FT sequence.

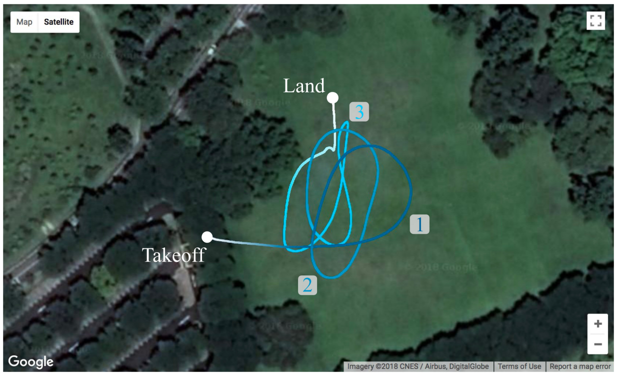

Fig. 25. Map overlay of the UAV flight in fixed wing mode.

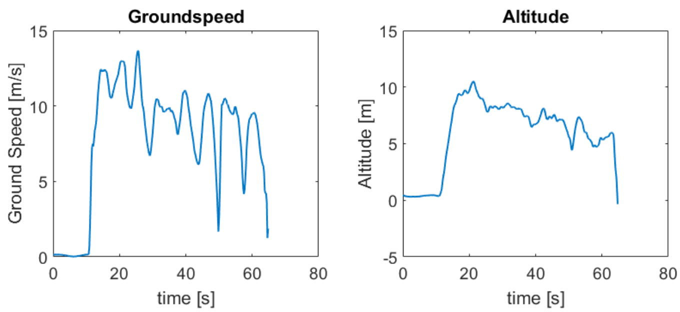

Fig. 26. Plots of the UAV ground speed and altitude.

of differential thrust for yaw control, we found that the craft is able to perform agile maneuvers- for example Maneuver 3 in Fig. 25 where the craft does a hairpin turn.

4. Conclusions and Future Work

It is our hope that this paper highlights the potential while also establishing the groundwork for future development of this unique hybrid configuration.

In terms of its potential, we showed that the THOR can achieve a near passive and controllable hover using the same aerodynamic surfaces that it would use for a controllable cruising flight. In fact, we were able to definitively observe that the craft used less throttle to stay airborne in both its hover and cruise flight configurations than if we attempted to hover purely through its propulsion systems.

In terms of groundwork, we described the specific design parameters that simplifies the challenges of modeling, stability and control. Most notable of these are the 2nd order rotational symmetry parameter, the fixed ω_z parameter and the separated cyclic and collective mechanism. It is worth noting that separated cyclic and collective also reduces the load on the actuators as now each actuator no longer needs to operate at both high torque and high speed. This gives us access to a greater variety of cheaper, smaller and lighter servos (coupled with a worm gear for when we need high torque) for the actuator mechanisms. Also in terms of groundwork, we have established a set of dynamic models that are simple but accurate for this novel design and implemented control solutions using PX4's open-source autopilot system.

Looking forward, we believe these contributions have opened the path in two areas. Firstly, we now believe we have sufficient material to develop figures of merit that would allow this platform to be effectively compared with other hybrid designs. While the reduced throttle in flight is a promising indication, we believe extensive work needs to be done to effectively compare the energy efficiencies and limits of this hybrid's flight envelope. This would possible entail specific wing designs based on the craft's intended missions. Secondly, we hope to look further into control solutions for the craft. Additional sensors (especially a more accurate altitude sensor due to the ground effect), feed-forward and/or non-linear control approaches and precession based control are interesting areas to explore that could compensate for the short-comings of the electronic swashplate. This shall be the focus of our future works.

A video compilation demonstrating the key flight movements discussed in this paper (hovering, FT, and cruising) of the prototypes can be found at `https://youtu.be/tBFndDLJKf0`.

Acknowledgments

This work was funded jointly by the SUTD-MIT International Design Centre and the Temasek Laboratories@SUTD, Singapore. The authors would like to thank Chee How Tan, Emmanuel Tang and Shawndy Lim for their enduring support and advice during the countless experiments that were necessary for the completion of this paper.

Appendix A. Flight Configurations

Table A.1. Configuration of THOR-Spartan.

Wing collective servo	None
Wing Flap Servo	MKS DS480
Flight Controller	PixRacer (with custom flight mode)
ESC	DJI Snail Brushless ESC
Motor	DJI Snail Motor
Propellers	DJI 5048 Tri-blade
Batteries	LiPo 3S 450 mah

Table A.1. (*Continued*)

Wing collective servo	None
Receiver	Spektrum + PixRacer WiFi
Wing Material	EPS Foam
Wing Span	500 mm
Weight	504 g
Hover Wing Angle	0.262 rad
ω_z Target	31.0 rad/s
ω_z PI Gain	0.0820, 0.0400
Collective P Gain	0.500
Cyclic P Gain	0.300

Table A.2. Configuration of THOR-Mini.

Wing collective servo	Actuonix P16-P
Wing Flap Servo	HiTec HS-40
Flight Controller	PixRacer (with custom flight mode)
ESC	DJI Snail Brushless ESC
Motor	Tiger Motor F40 Pro II 1600kv
Propellers	DJI 5048 Tri-blade
Batteries	LiPo 3S 450 mah
Receiver	Spektrum + PixRacer WiFi
Wing Material	Onyx Carbon Fiber Filament
Wing Span	300 mm
Weight	540 g
Hover Wing Angle	0.262 rad
ω_z Target	33 rad/s
ω_z PI Gain	0.0820, 0.0120
Collective P Gain	0.500
Cyclic P Gain	0.300

References

[1] Norton and Bill, *Bell Boeing V-22 Osprey, Tiltrotor Tactical Transport*, Midland Publishing (Earl Shilton, Leicester, UK, 2004).

[2] Frawley and Gerald, *The International Directory of Military Aircraft*, Aerospace Publications (Fyshwick, ACT, Australia, 2002).

[3] A. Kellas, The guided samara: Design and development of a controllable single-bladed autorotating vehicle, *Thesis, Department of Aeronautics and Astronautics*, Massachusetts Institute of Technology (Boston, Massachusetts, 2007).

[4] D. Lentink, W. B. Dickson, J. L. van Leeuwen and M. H. Dickinson, Leading-edge vortices elevate lift of autorotating plant seeds, *Science* **324**(5933) (2009) 1438–1440 (American Association for the Advancement of Science, Washington, D.C. 2009).

[5] A. Papin and D. Rouilly, "Helicopter", U.S. Patent 1 133 660, March 30, 1915.

[6] J. Houghton and W. Hobrug, Fly-by-wire control of a monocopter, experimental projects II technical report, Massachusetts Institute of Technology (Boston, Massachusetts, 2008).

[7] H. Youngren, S. Jameson and B. Satterfield, in Design of the SAMARAI monowing rotorcraft nano air vehicle, in *Proc. American Helicopter Society 65th Annual Forum* (Grapevine, Texas, 2009), pp. 684–697.

[8] C. Hockley and B. Butka, The samareye: A biologically inspired autonomous vehcile, in *Proc. 29th Digital Avionics Systems Conference* (Salt Lake City, Utah, 2010), pp. 5-C.

[9] S. Verling, B. Weibel, M. Boosfeld, K. Alexis, M. Burri and R. Siegwart, Full attitude control of a VTOL tailsitter UAV, in *Proc. IEEE Int. Conf. Robotics and Automation* (Stockholm, Sweden, 2016), pp. 3006–3012.

[10] R. Ritz and R. D'Andrea, in A global controller for flying wing tailsitter vehicles, in *Proc. IEEE Int. Conf. Robotics and Automation* (Singapore, Singapore, 2017), pp. 2731–2738.

[11] J. E. Low, L. T. S. Win, D. S. B. Shaiful, C. H. Tan, G. S. Soh and S. Foong, Design and dynamic analysis of a Transformable Hovering Rotorcraft (THOR), in *Proc. IEEE Int. Conf. Robotics and Automation* (Singapore, Singapore, 2017), pp. 6389–6396.

[12] J. E. Low, L. T. S. Win, J. L. Lee, G. S. Soh and S. Foong, Towards a stable three-mode Transformable HOvering Rotorcraft (THOR) in *Proc. IEEE Int. Conf. Advanced Intelligent Mechatronics* (Auckland, New Zealand, 2018), pp. 492–497.

[13] D. Sufiyan, L. T. S. Win, J. E. Low, S. K. H. Win, G. S. Soh and S. Foong, Optimized transition path of a Transformable HOvering Rotorcraft (THOR) in *Proc. IEEE Int. Conf. Advanced Intelligent Mechatronics* (Auckland, New Zealand, 2018), pp. 460–465.

[14] K. Fregene and C. L. Bolden, Dynamic and control of a biomimetic single-wing nano air vehicle, in *Proc. American Control Conf.* (Baltimore, Maryland, 2010), pp. 51–56.

[15] E. R. Ulrich, D. J. Pines and J. S. Humbert, From falling to flying: The path to powered flight of a robotic samara nano air vehicle, *J. Bioinspiration & Biomimetics* **5**(4) (2010) 1–16.

[16] G. Matic, M. Topic and M. Jankovec, Mathematical model of a monocopter based on unsteady blade-element momentum theory, *J. Aircr.* **52**(6) (2015) 1–9.

[17] M. S. Ashbaugh, C. C. Chicone and R. H. Cushman, The twisting tennis racket, *J. Dyn. Differ. Equ.* **3**(1) (1991) 67–85.

[18] G. M. Hoffmann, H. Huang, S. L. Waslander and C. J. Tomlin, Quadrotor helicopter flight dynamics and control: Theory and experiment, *AIAA Guidance, Navigation and Control Conference and Exhibit* (Hilton Head, South Carolina, August 2007), Stanford University.

[19] J. G. Leishman, *Principles of Helicopter Aerodynamics*, 3rd edn., Michael J. Rycroft and Robert F. Stengel (eds.) (Cambridge University Press, Cambridge, United Kingdom, 2002).

[20] R. W. Prouty, *Helicopter Performance, Stability, and Control*, 2002 edn. (Krieger Pub Co, 2001).

[21] R. Ritz and R. D. Andrea, *A Global Strategy for Tailsitter Hover Control, Robotics Research* (Springer, Cham, 2018), pp. 21–37.

[22] M. E. Argyle, R. W. Beard and S. Morris, The vertical bat tail-sitter: dynamic model and control architecture, *American Control Conf. (ACC), 2013* (IEEE, 2013), pp. 806–811.

[23] R. E. Sheldahl and P. C. Klimas, Aerodynamic characteristics of seven symmetrical airfoil sections through 180-degree angle of attack for use in aerodynamic analysis of vertical axis wind turbines, *Techical Report*, Sandia National Labs., Albuquerque, NM (USA) (1981).

[24] D. Brescianini, M. Hehn and R. DAndrea, Nonlinear quadrocopter attitude control: Technical Report, ETH Zurich (2013).

[25] L. Meier, D. Honegger and M. Pollefeys, Px4: A nodebased multithreaded open source robotics framework for deeply embedded platforms, *2015 IEEE International Conference on Robotics and Automation (ICRA)* (IEEE, 2015), pp. 6235–6240.

[26] J. Diebel, Representing attitude: Euler angles, unit quaternions, and rotation vectors, *Matrix* **58**(15–16) (2006) 135.

[27] L. Meier, J. Camacho, B. Godbolt, J. Goppert, L. Heng, M. Lizarraga *et al.*, Mavlink: Micro air vehicle communication protocol, Online]. Tillganglig: http://qgroundcontrol.org/mavlink/start.[Hamtad 2014-05-22] (2013).

Jun En Low received his B.Eng from the Singapore University of Technology and Design (SUTD) in 2015. His research interests are in dynamic modeling and robotic control, in particular, the symbiotic integration of hardware and software solutions that improve the robustness of system control.

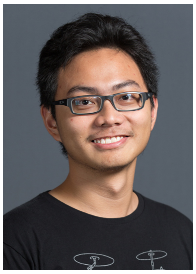

Danial Sufiyan received his B.Eng from the Singapore University of Technology and Design (SUTD) in 2016 and is continuing on for his Ph.D. His research interests include unconventional and nature-inspired Unmanned Aerial Vehicles (UAVs), control, simulation and visualization, as well as machine learning for UAV design and control applications.

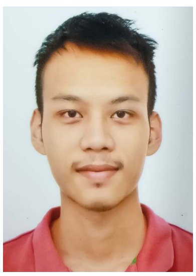

Luke Soe Thura Win is currently a Research Officer at the Singapore University of Technology and Design (SUTD). He received his B.E. in Electrical & Electronics Engineering from Nanyang Technological University (NTU) in 2014. His research contributions have focused on the design of various unmanned vehicles with a specialization in integrating control and sensing solutions on unconventional aerial platforms. His research interests are in nature-inspired robotics and rapid prototyping methodologies.

Gim Song Soh is an Assistant Professor in the Engineering Product Development Pillar at Singapore University of Technology and Design. He obtained his M.Sc. and Ph.D. degree from University of California, Irvine (UCI), where he researched and developed innovative computer aided design software tools for the invention of articulated mechanical systems. His research interests lies on mechanism and robotics with emphasis on its design, kinematics and biomechanics.

Shaohui Foong is an Associate Professor in the Engineering Product Development (EPD) pillar at the Singapore University of Technology and Design (SUTD) and Visiting Academician at the Changi General Hospital, Singapore. He received his B.S., M.S. and Ph.D. degrees in Mechanical Engineering from the George W. Woodruff School of Mechanical Engineering, Georgia Institute of Technology, Atlanta, USA. In 2011, he was a Visiting Assistant Professor at the Massachusetts Institute of Technology, Cambridge, USA. His research interests include system dynamics control, nature-inspired robotics, magnetic localization, medical devices and design education pedagogy.